Experimental Demonstration of Soft-ROADMs with Dual-Arm Drop Elements for Future Optical-Wireless Converged Access Networks

Gonem, Omaro; Giddings, Roger; Tang, Jianming

Journal of Lightwave Technology

Published: 15/03/2024

Peer reviewed version

Experimental Demonstration of Soft-ROADMs with Dual-Arm Drop Elements for Future Optical-Wireless Converged Access Networks

Omaro Fawzi Abdelhamid Gonem, Roger Philip Giddings, and Jianming Tang

***Abstract*— Digital signal processing (DSP)-enabled soft reconfigurable optical add/drop multiplexers (Soft-ROADMs) offer flexible add/drop optical switching at wavelength, sub-wavelength and spectrally-overlapped orthogonal (I and Q) sub-band (SB) levels, which makes them highly desirable for enabling flexible reconfigurable optical-wireless converged access networks where both fixed and wireless access services are consolidated in a shared network, enabling network resource efficient and cost-effective connectivity solutions. However, the performance of the targeted sub-band (TSB) extracted by the soft-ROADM drop element is extremely sensitive to drop RF signal phase offset, which is a major limitation impacting the technical feasibility of soft-ROADMs. To overcome this challenge, in this paper, a phase-offset-insensitive soft-ROADM dual-arm IQ drop operation is proposed and experimentally demonstrated. A DSP implemented multi-input multi-output (MIMO)-based I/Q crosstalk mitigation technique is employed to achieve the insensitivity to drop RF signal phase offset. It is shown that, the traditional single-arm I/Q soft-ROADM drop element has a limited drop RF signal phase offset dynamic range of $\sim \pm \pi/4$ ($< \pm 0.05\pi$) in the presence of I/Q (I&Q) SBs, thus requiring accurate phase control, however, the proposed dual-arm IQ drop element demonstrates the ability to tolerate any arbitrary phase offset, thus completely eliminating the need to dynamically control the drop RF signal's phase. This paper also experimentally demonstrates the effectiveness of the new dual-arm drop element to mitigate any I/Q crosstalk effects caused by, various effects, including the fiber transmission channel-induced frequency response roll-off, symbol timing offset, and propagation delay drifting effects. Importantly, it is shown that the traditional single-arm I/Q drop element offers poor performance stability as the dropped TSB's BER performance degrades within a few minutes, whereas, the new dual-arm drop element achieves a highly stable BER performance. Soft-ROADMs incorporating the newly proposed dual-arm IQ drop element are thus experimentally shown to offer significantly reduced implementation complexity, thus radically increasing their suitability for application in optical-wireless converged access networks.**

***Index Terms*— 5G, digital filtering, digital signal processing (DSP), optical-wireless converged access networks, reconfigurable optical add/drop multiplexer (ROADM), timing offset.**

I. Introduction

The unprecedented growth in mobile internet-based applications with widely diverse connectivity requirements, along with the prediction that 65% of the world's global population will have 5G connectivity by the end of 2025 [1], are driving the demand for future advanced 5G/6G transport networks with enhanced capacity, lower latency and significantly improved network reconfigurability to enable great flexibility and adaptability to efficiently deliver the different services with varying connectivity demands [2]. Additionally, the vision of future 6G networks is to enhance key capabilities to support a diverse range of new time-sensitive services (TSSs) and real-time applications (RTAs), offering a peak data rate of ≥1 Tbps, massive connection density of 10 million devices/km^2 and ultra-low latency of 10–100 μs [3]. This necessitates the seamless integration of fixed optical access networks and wireless radio access networks (RANs) to realise cost-effective network deployment via highly efficient and dynamic utilisation of network resources [4]. In addition, this also emphasizes the pressing need to fully incorporate metro networks with the access networks to achieve seamlessly converged metro-access solutions with ultra-low latency and high power efficiency [5], [6].

The current fronthaul connectivity between remote radio units (RRUs) and centralized baseband units (BBUs) in the existing 5G centralised RANs (C-RANs) is typically static and inflexible which hinders the reconfigurability and adaptability of the network [7]. Additionally, the current metro networks are based on wavelength-switched point-to-point (PTP) links [8], [9]. It is envisaged that future seamlessly converged access and metro networks must incorporate unified, dynamic, adaptable and reconfigurable point-to-multipoint (PTMP) connectivity, controlled via software-defined networking (SDN), which allows both fixed data and fronthaul services to be consolidated to meet the aforementioned evolving advanced transport network demands [10], [11].

Recent years have witnessed growing research interest in developing reconfigurable optical add/drop multiplexers (ROADMs) as key network devices, as ROADMs offer dynamic on-demand network reconfigurability due to their wavelength switching functionality with the ability to optimally allocate and/or re-allocate wavelength resources according to the prevailing traffic requirements allowing for efficient resource utilization and fast adaptability. ROADMs can also

Manuscript received xxxxxxx xx, 2023; revised xxxxx xx, 2023. This work was supported by the DSP Centre of Excellence funded by the European Regional Development Fund (ERDF) through the Welsh Government. (Corresponding author: Roger Philip Giddings).

The authors are with the School of Computer Science and Electronic Engineering, Bangor University, Bangor, LL57 1UT, UK. (email: o.gonem@bangor.ac.uk; r.p.giddings@bangor.ac.uk; j.tang@bangor.ac.uk)

reduce latency as they eliminate the need for intermediate optical-electrical-optical (O-E-O) conversions and electronic switching [12]–[14]. Moreover, ROADMs provide the capability to choose the optimal traffic path within the optical network which not only optimizes the network performance, but can potentially aid in achieving ultra-low latency, as routes with lower total propagation delay can be selected. The aforementioned ROADMs' advantages, thus make them attractive network devices for achieving reconfigurable, ultra-low latency, optical-wireless converged access networks [7].

While ROADM technologies have evolved significantly over the past decade, the improvements have mainly focused on enhancing the functionalities in terms of colourless, directionless, and contentionless (CDC) and CDC gridless (CDCG) capabilities. However, these improvements have come at a significant increase in cost and complexity [15]–[19]. Moreover, existing ROADMs have a fixed wavelength level optical switching granularity, thus each network connection must be allocated a complete wavelength resource, regardless of the prevailing traffic load, which can lead to excessively low network utilisation efficiency when traffic loading is low. This restricts the flexibility, dynamic adaptability, and cost-effectiveness of the existing ROADMs for future optical-wireless converged access networks.

To address the abovementioned technical challenge, cost-effective digital signal processing (DSP)-based, software-reconfigurable, digital filter multiplexing (DFM)-enabled [20], O-E-O conversion-free and optical filter-free, SDN-controllable ROADMs, termed soft-ROADMs, have been recently proposed and experimentally demonstrated, to offer enhanced flexibility, finer optical switching granularity, cost-effectiveness and increased dynamic reconfigurability in both access and metro networks.

Soft-ROADMs offer several salient features over the existing ROADMs, key features include i) greatly enhanced network flexibility, adaptability and reconfigurability due to their ability to offer dynamic on-demand add/drop optical switching at the wavelength level, the sub-wavelength (SW) and spectrally-overlapped orthogonal In-phase (I) and/or Quadrature-phase (Q) sub-band (SB) levels, ii) enhanced network elasticity due to the ability to support dynamically varying SW/SB bandwidths, and iii) high spectral efficiency per wavelength due to their ability to simultaneously and dynamically accommodate multiple SW/SBs (data channels) on the same wavelength resource.

Ultra-dense wavelength switched networks (UD-WSNs) [21]–[23] employing ROADMs with fine spectral resolution wavelength selective switches (WSSs) have been proposed to improve the overall spectral efficiency of metro networks, as the frequency slots (FSs) in UD-WSNs are of the order of 12.5 GHz or 6.25 GHz. Soft-ROADMs are fully compatible with UD-WSNs allowing even fine sub-FS switching granularity. On the other hand, as the soft-ROADMs offer a basic networking solution of using electrical signals to dynamically control optical signals without involving O-E-O conversion, thus they may play a significant role in seamlessly converging metro and access networks.

The soft-ROADMs' performance has been comprehensively numerically investigated using different signal modulation formats in both intensity modulation and direct detection (IMDD)-based [24], [25] and coherent [26] transmission systems. Furthermore, experimental demonstrations of the soft-ROADM's performance have been reported [27], [28]. Additionally, the technical feasibility of the soft-ROADM in real-time DSP-based systems has been experimentally demonstrated [29]. The soft-ROADM leverages a cost-efficient add operation using passive optical couplers. Whereas the soft-ROADM drop operation is based on an optical intensity modulation operation on the input optical signal using an optical intensity modulator (IM) driven by an SDN-controllable sinusoidal drop RF signal. However, as experimentally observed in [29], the performance of the targeted SB (TSB) extracted by the soft-ROADM drop element is extremely sensitive to phase offsets in the drop RF signal, as any deviation of the drop RF signal phase from the optimum phase results in I/Q crosstalk between spectrally overlapped orthogonal I and Q SBs leading to the reduction of the optical signal to noise ratio (OSNR) of the TSB [29]. Thus, to achieve acceptable TSB performance and stability, a feedback-based phase control scheme could be employed, which, however, has the challenge that costly discrete RF components are needed with suitable DSP control algorithms still necessary. Therefore, a simple and low cost solution is needed to dynamically control the drop RF signal's phase or else mitigate its effect.

To address the abovementioned technical challenge, this paper presents a novel dual-arm IQ soft-ROADM drop element employing a new multi-input multi-output (MIMO)-based I/Q crosstalk mitigation technique to eliminate the soft-ROADM drop RF signal phase offset effects. It is shown that, for the adopted conditions, the single-arm I/Q drop element shows a limited drop RF signal phase offset dynamic range of $\sim \pm \pi/4$ ($< \pm 0.05\pi$) in the presence of I/Q (I and Q) SBs, whereas the proposed dual-arm IQ drop element achieves a phase-offset-insensitive bit error ratio (BER) performance, thus totally eliminating the need to dynamically control the drop RF signal's phase. In addition, the results experimentally confirm the ability of the new dual-arm IQ drop element in mitigating any I/Q crosstalk effects induced as a result of; the fiber transmission channel-induced frequency response roll-off, symbol timing offset (STO) between transmitter and receiver, and fiber propagation delay drifting effects. In comparison, the single-arm I/Q drop element shows poor tolerance to I/Q crosstalk effects. For example, for the single-arm I/Q drop element the BER can degrade within a few minutes, whereas the proposed dual-arm IQ drop element achieves a highly stable BER performance. Therefore, the proposed dual-arm IQ soft-ROADM drop element is experimentally validated to offer high resilience to I/Q crosstalk effects and reduced implementation complexity, making it highly suitable for application in optical-wireless converged access networks.

II. Operating Principle of Soft-ROADMs with Dual-Arm IQ Drop Elements

Fig. 1 illustrates a dynamically reconfigurable optical-

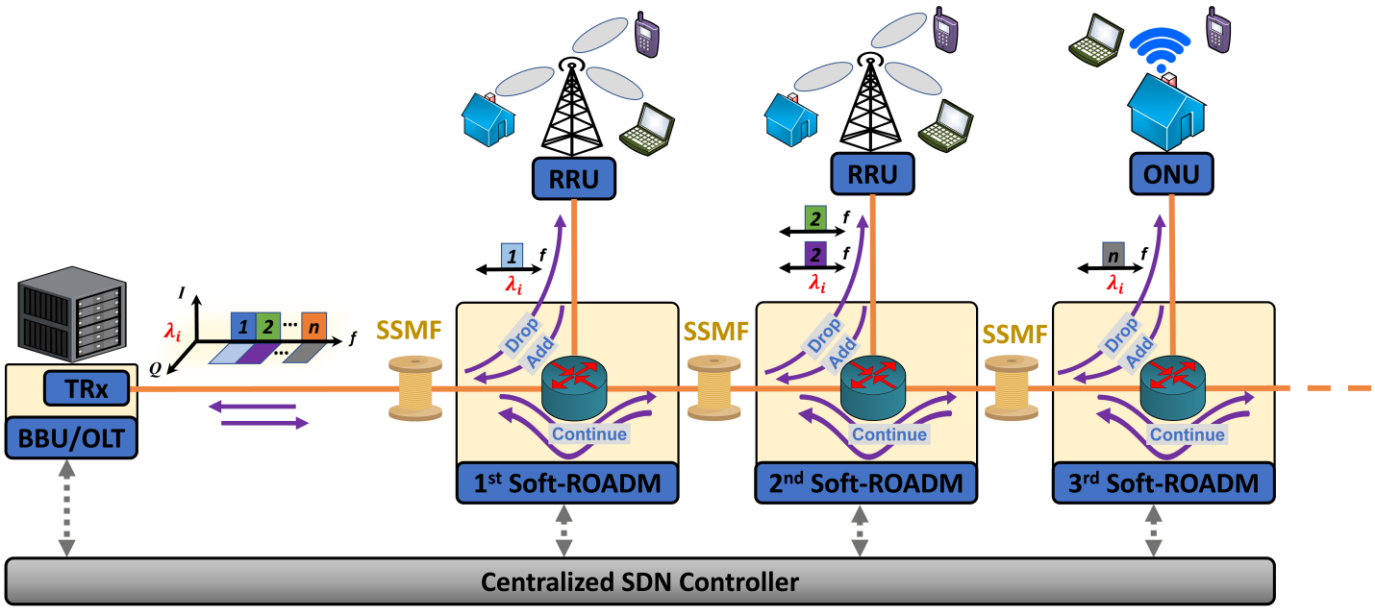

Fig. 1. Schematic diagram of the optical-wireless converged access network enabled by soft-ROADMs. ONU: optical network unit, OLT: optical line terminal, BBU: baseband unit, RRU: remote radio unit, SSMF: standard single-mode fiber, TRx: transceiver.

wireless converged access network enabled by soft-ROADMs, this scenario is considered in this paper to demonstrate that, similar to PTMP coherent XR optics [9], [30], the deployment of soft-ROADMs offers the potential for cost-effective migration from PTP BBU-RRU links towards cost-effective PTMP connectivity [13] with improved flexibility and adaptability. Thus, a single centralised high-speed transceiver utilizing the DSP-enabled DFM technique [20], is used to simultaneously receive/send multiple independent signals from/to multiple lower-speed soft-ROADM add/drop element-based transceivers via a single wavelength. Moreover, the DFM-based SBs, can be dynamically allocated to carry either mobile fronthaul traffic i.e., BBU to RRU or fixed data traffic i.e., optical line terminal (OLT) to optical network unit (ONU). Also, the SBs can have dynamically varying bandwidths (capacity) and be adaptively switched to different RRUs/ONUs as required, thus supporting adaptive network reconfiguration to effectively manage dynamic traffic patterns. In addition, considering the downstream direction, the digital-to-analogue converters (DAC) at the BBU/OLT must support the full bandwidth of the aggregated SBs, however the analogue-to-digital converter (ADC) at the RRUs/ONUs only needs to support the maximum SB bandwidth, as discussed later, which is highly desirable for the practical realization of low-cost RRUs/ONUs. Furthermore, it is also possible to support various passive network topologies, such as ring topology, via the use of simple passive splitters and the network can also be designed to provide redundancy and thus protect against network link failures.

Fig. 2 shows the schematic diagram of the soft-ROADM architecture which is fully compatible with SDN-based network management. Detailed descriptions of the soft-ROADM operating principle can be found in [25]. As illustrated in Fig. 2, for a specific wavelength, the soft-ROADM add operation at any level is achievable using a simple passive coupler where the centralized SDN controller communicates with the soft-ROADM-embedded local DSP controller to supervise the add operation to avoid any possible channel contentions.

Fig. 3 shows the architecture of the newly proposed dual-arm IQ soft-ROADM drop element which is compatible with any transmission system employing single or multi-carrier-based modulation. In contrast to the single-arm I/Q soft-ROADM drop element [29], which drops a single I or Q TSB making it very sensitive to any I/Q crosstalk effects, the newly proposed dual-arm IQ drop element achieves an I/Q crosstalk-tolerant drop operation. This is achieved by simultaneously dropping both orthogonal I and Q TSBs and jointly processing them with a purely DSP implemented MIMO-based I/Q crosstalk mitigation technique which is explained in detail in Section III. The proposed dual-arm IQ soft-ROADM drop element employs two IMs and a DSP-based IQ receiver to achieve a linear 2×2 MIMO system to realize the I/Q crosstalk mitigation. A single SDN-controllable drop RF signal source and a 90° phase shifter are employed to generate the orthogonal I and Q drop RF signals required to drive the two IMs.

As illustrated in Fig. 3, the incoming optical signal is passively split to produce two signals to simultaneously feed the I and Q arms of the drop element. The optical signal in the I (Q) arm passes through an optimally DC-biased optical IM driven with the drop RF signal. When the drop RF signal is adjusted to match the I (Q) TSB signal in both RF frequency and phase, the I (Q) TSB is then shifted to the baseband region with a reversed spectrum at the output of the IM, while all other non-targeted SBs (n-TSBs) of the same wavelength are ruined and unrecoverable. A simple analogue low-pass filter (LPF) is then employed after the direct detection photodetector and before the ADC to separate TSB from the ruined SBs. This allows the dual-arm IQ drop element electronics to operate at the bandwidth of the TSBs, offering the aforementioned significant relaxation of the required ADC sampling speed and

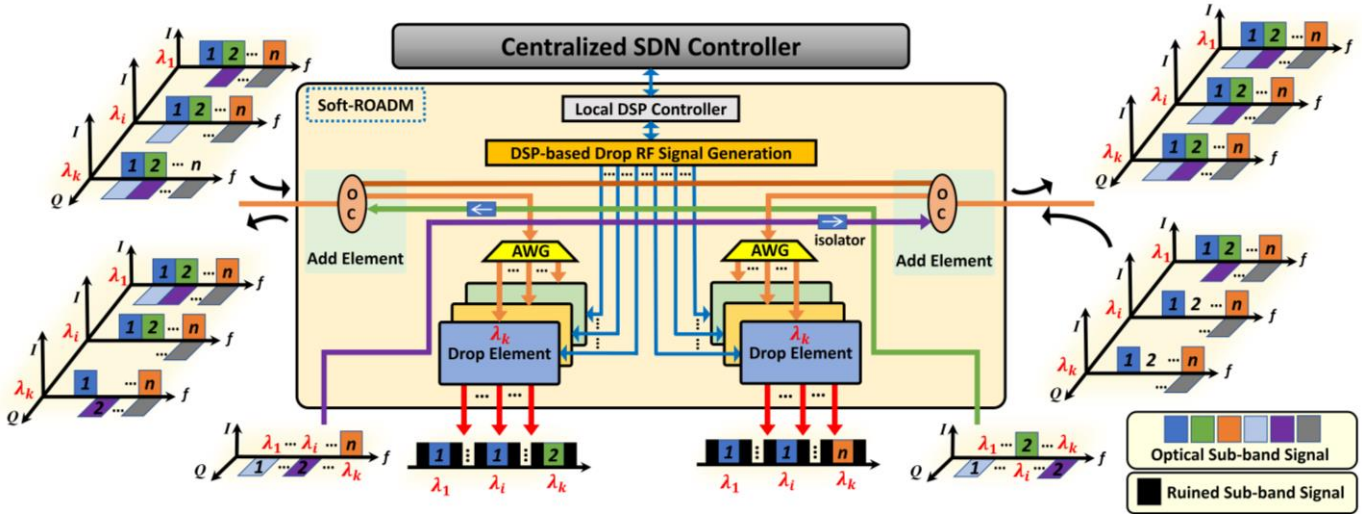

Fig. 2. Schematic diagram of DSP-enabled soft-ROADM supporting the SDN solution, AWG: arrayed waveguide grating, OC: optical coupler.

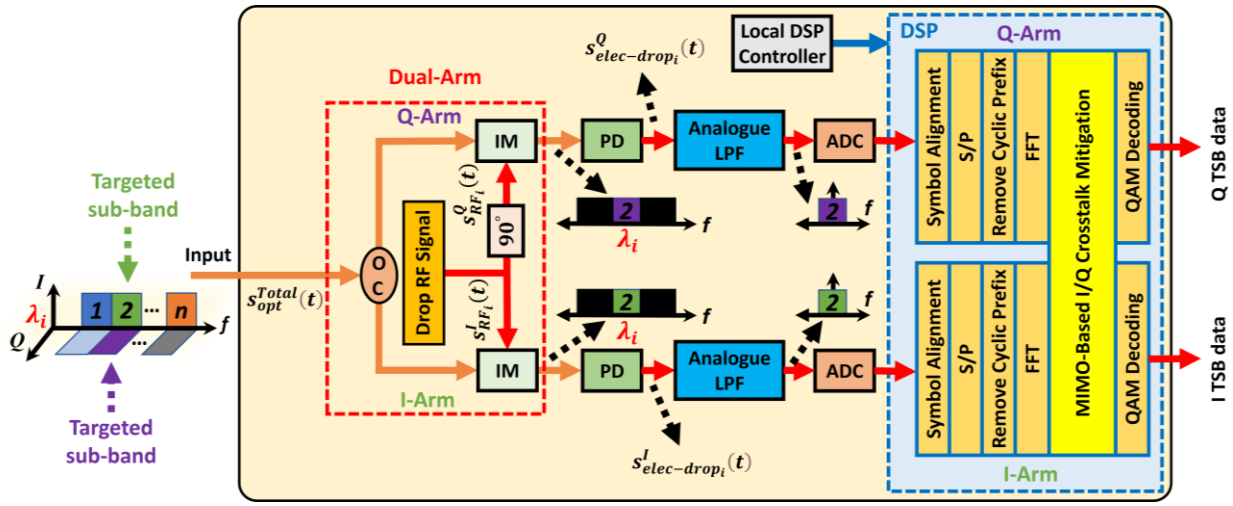

Fig. 3. Proposed dual-arm IQ soft-ROADM drop element. OC: optical coupler, IM: intensity modulator, PD: photodetector, LPF: low-pass filter, ADC: analogue-to-digital converter, S/P: serial-to-parallel conversion, FFT: fast Fourier transform.

eliminating the need for further digital filtering. The output signals of both arms are then jointly processed in the DSP-based IQ receiver employing the MIMO-based I/Q crosstalk mitigation technique after individual fast Fourier transform (FFT) operations and before data recovery in each arm.

As 6G may require latencies as low as 10 µs, it is important to discuss soft-ROADM DSP-induced latency. The processing latency in the dual-arm IQ drop element is mainly due to the two parallel FFT operations, thus the total latency equals that of one FFT. As an indication of FFT latency, a 256-point FFT has been achieved with a latency as low as 46 ns [31]. In addition, as the latency increases with FFT size, adopting the SB level processing requires a smaller FFT size and thus lowers the latency, compared to the FFT required to process the whole aggregated signal [32]. Furthermore, the latency associated with the MIMO-based I/Q crosstalk mitigation technique is based on matrix multiplication, i.e. parallel multipliers and adders, adding a delay of only a few clock cycles. As a result, the overall DSP latency could be a few 100 ns, which is significantly below the latency target of 6G networks.

It is also important to note that silicon photonic integrated circuits (PICs) can potentially be exploited to enable the practical realization of low-cost soft-ROADMs [33], [34].

III. MIMO-Based I/Q Crosstalk Mitigation Technique

A. I/Q Crosstalk due to Drop RF Signal Phase Offset

To highlight the impact of I/Q crosstalk due to drop RF signal phase offset, and to simplify the theoretical analysis, ideal digital shaping filter responses and IMs are assumed in this section. In the BBU/OLT-based transmitter, the generated DFM-based real-valued electrical signals for I and Q SBs occupying the i^{th} SW-band can be approximated as:

$$s_i^I(t) = a_i^I(t)\cos\left(2\pi f_{c_i} t\right) \quad (1)$$

$$s_i^Q(t) = a_i^Q(t)\sin\left(2\pi f_{c_i} t\right) \quad (2)$$

where $a_i^I(t)$ and $a_i^Q(t)$ are the I and Q SB data signals of the i^{th} SW-band respectively, f_{c_i} is the central frequency of the digital filters where:

$$f_{c_i} = [2i-1] \times f_{DAC}/(2M) \quad (3)$$

where f_{DAC} is the effective DAC sampling speed, and M is the up-sampling factor, adopted in the DFM-based transmitter. The total transmitter side optimum DC-biased, real-valued electrical signal containing u SW-bands is:

$$s_{elec}^{Total}(t) = \left[\sum_{i=1}^{u}\sum_{w=\{I,Q\}} s_i^w(t)\right] + v \quad (4)$$

where v is the optimum DC bias current. For a specific optical carrier frequency, f_o, the total transmitted optical signal containing u SW-bands at the output of an ideal IM can be described as:

$$s_{opt}^{Total}(t) = \sqrt{s_{elec}^{Total}(t)}e^{j2\pi f_o t} \quad (5)$$

For the soft-ROADM drop operation of I and Q SBs in the i^{th} SW-band, the drop RF signals for I and Q arms are:

$$s_{RF_i}^I(t) = \cos\left(2\pi f_{c_i} t + \theta_{RF_i}\right) + v_{RF_i}^I \quad (6)$$

$$s_{RF_i}^Q(t) = \sin\left(2\pi f_{c_i} t + \theta_{RF_i}\right) + v_{RF_i}^Q \quad (7)$$

where $v_{RF_i}^I$ and $v_{RF_i}^Q$ are the optimum DC bias current for I and Q arms respectively, and θ_{RF_i} is the drop RF signal phase offset relative to the ideal phase.

The optical signals at the output of the dual-arm IQ drop element's IMs in Fig. 3, can be expressed as:

$$s_{opt-drop_i}^w(t) = \sqrt{s_{RF_i}^w(t)}s_{opt}^{Total}(t), \quad (w = I, Q) \quad (8)$$

For simplicity, we only consider the drop RF signal and the optical signals in the same i^{th} SW-band since the mixing between the i^{th} drop RF signal and other n-TSBs results in ruined and unrecoverable signal bands that are removed by filtering, therefore:

$$s_{opt-drop_i}^I(t) = \sqrt{s_{RF_i}^I(t)s_i^I(t) + s_{RF_i}^I(t)s_i^Q(t)}\, e^{j2\pi f_o t} \quad (9)$$

$$s_{opt-drop_i}^Q(t) = \sqrt{s_{RF_i}^Q(t)s_i^I(t) + s_{RF_i}^Q(t)s_i^Q(t)}\, e^{j2\pi f_o t} \quad (10)$$

After direct detection in each arm, ignoring noise effects, the resultant electrical signal for I/Q SB in the i^{th} SW-band is represented as:

$$s_{elec-drop_i}^I(t) = \beta_i^I\left[s_{RF_i}^I(t)s_i^I(t) + s_{RF_i}^I(t)s_i^Q(t)\right] \quad (11)$$

$$s_{elec-drop_i}^Q(t) = \beta_i^Q\left[s_{RF_i}^Q(t)s_i^I(t) + s_{RF_i}^Q(t)s_i^Q(t)\right] \quad (12)$$

where β_i^I and β_i^Q take into account all signal losses during optical-to-electrical (O-E) conversions. The terms $s_{RF_i}^I(t)s_i^I(t)$ and $s_{RF_i}^Q(t)s_i^Q(t)$ are the desired I and Q TSBs respectively, whereas the terms $s_{RF_i}^I(t)s_i^Q(t)$ and $s_{RF_i}^Q(t)s_i^I(t)$ denote inter-sub-band leakage components between the I and Q SBs in the i^{th} SW-band.

After suitable analogue LP filtering, the electrical baseband dropped TSBs in Eqs. (11) and (12) can be expressed as:

$$s_{elec-drop_i}^I(t) = \beta_i^I\left[a_i^I(t)\cos\left(\theta_{RF_i}\right) - a_i^Q(t)\sin\left(\theta_{RF_i}\right)\right] \quad (13)$$

$$s_{elec-drop_i}^Q(t) = \beta_i^Q\left[a_i^I(t)\sin\left(\theta_{RF_i}\right) + a_i^Q(t)\cos\left(\theta_{RF_i}\right)\right] \quad (14)$$

Equations (13) and (14) show that θ_{RF_i} causes an I/Q crosstalk effect, consisting of power loss, proportional to $\cos\left(\theta_{RF_i}\right)$, within the dropped TSB and inter-SB leakage proportional to $\sin\left(\theta_{RF_i}\right)$. In addition, all SBs are equally affected by θ_{RF_i} regardless of their spectral location, and all frequency components of a SB are also equally affected. In addition, for any value of θ_{RF_i}, Eqs. (13) and (14) imply that any power loss of I (Q) SB in the I (Q) arm appears as power leakage in the Q (I) arm. Thus, depending on θ_{RF_i}, each arm of the dual-arm and the single-arm I/Q drop element, receives different power combinations of the I and Q SBs. This suggests that the single-arm data recovery approach cannot mitigate any drop RF signal phase offset effects as the particular power combination of I and Q is unknown.

B. MIMO-Based I/Q Crosstalk Mitigation Technique

The single-arm I/Q drop element assumes that, for any transmission system consisting of an arbitrarily modulated single carrier ($k = 1$) or multiple subcarriers ($k > 1$) located in a given SB, the received I or Q data for the k^{th} subcarrier is:

$$y_{k,i}^I = h_{k,i}^{II}x_{k,i}^I + w_{k,i}^I \quad (15)$$

$$y_{k,i}^Q = h_{k,i}^{QQ}x_{k,i}^Q + w_{k,i}^Q \quad (16)$$

where $y_{k,i}^I$ ($y_{k,i}^Q$) are the received encoded data symbols conveyed by the k^{th} received subcarrier in the single-arm I (Q) drop element. $x_{k,i}^I$ and $x_{k,i}^Q$ are the transmitted encoded data symbols conveyed by the k^{th} subcarriers of I and Q SBs in the i^{th} SW-band respectively. $h_{k,i}^{II}$ and $h_{k,i}^{QQ}$ are the intra-SB channel coefficients, and $w_{k,i}^I$ and $w_{k,i}^Q$ represent noise. The single-arm I/Q drop element employs the conventional pilot-based subcarrier channel estimation and equalization techniques for data recovery [35], [36] which cannot compensate the I/Q crosstalk effect.

To solve this issue, the proposed MIMO-based I/Q crosstalk mitigation technique accounts for the fact that for any subcarrier k, each received data symbol is a combination of both I and Q SBs. The received I and Q frequency-domain data symbols are:

$$y_{k,i}^I = h_{k,i}^{II}x_{k,i}^I + h_{k,i}^{IQ}x_{k,i}^Q + w_{k,i}^I \quad (17)$$

$$y_{k,i}^Q = h_{k,i}^{QI}x_{k,i}^I + h_{k,i}^{QQ}x_{k,i}^Q + w_{k,i}^Q \quad (18)$$

where $h_{k,i}^{IQ}$ and $h_{k,i}^{QI}$ are the inter-SB channel coefficients. Eqs. (17) and (18) can be regarded as a system of linear equations, with the same structure as a 2×2 MIMO system, thus the received I and Q data symbols can be jointly processed to recover the transmitted I and Q data symbols. The matrix representation of Eqs. (17) and (18) is:

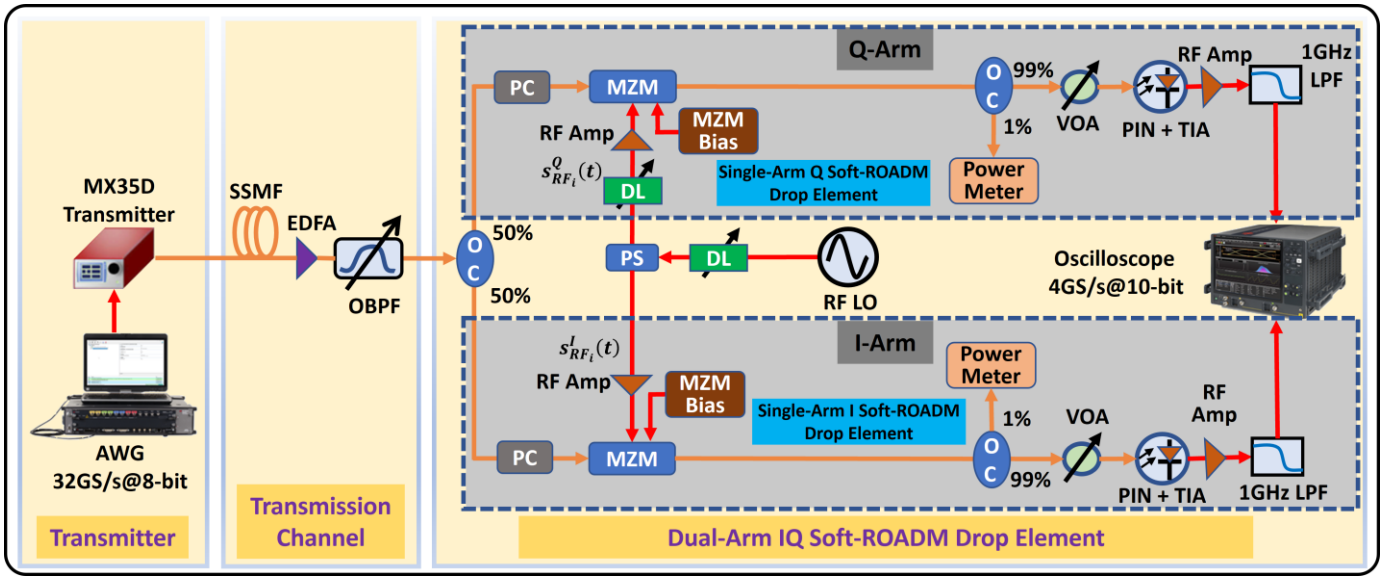

Fig. 4. Experimental setup of the proposed dual-arm IQ soft-ROADM drop element. AWG: arbitrary waveform generator, SSMF: standard single-mode fiber, EDFA: Erbium-doped fiber amplifier, OBPF: optical band-pass filter, PC: polarization controller, MZM: Mach-Zehnder modulator, PS: power splitter, OC: optical coupler, DL: delay line, VOA: variable optical attenuator, LPF: low-pass filter.

$$\begin{bmatrix} y_{k,i}^{I} \\ y_{k,i}^{Q} \end{bmatrix} = \begin{bmatrix} h_{k,i}^{II} & h_{k,i}^{IQ} \\ h_{k,i}^{QI} & h_{k,i}^{QQ} \end{bmatrix} \begin{bmatrix} x_{k,i}^{I} \\ x_{k,i}^{Q} \end{bmatrix} + \begin{bmatrix} w_{k,i}^{I} \\ w_{k,i}^{Q} \end{bmatrix} \tag{19}$$

which is:

$$\boldsymbol{y_{k,i}} = \boldsymbol{H_{k,i}}\boldsymbol{x_{k,i}} + \boldsymbol{w_{k,i}} \tag{20}$$

where $\boldsymbol{y_{k,i}}$ is the 2×1 vector of received encoded data conveyed on the k^{th} subcarrier of the i^{th} SW-band, $\boldsymbol{x_{k,i}}$ is the 2×1 transmitted signal vector, $\boldsymbol{H_{k,i}}$ the is 2×2 MIMO sub-band channel coefficients matrix, and $\boldsymbol{w_{k,i}}$ is the 2×1 noise vector.

To estimate the MIMO sub-band channel coefficients matrix, we consider a set of J training symbols $\boldsymbol{p_{1_{k,i}}}, \ldots, \boldsymbol{p_{J_{k,i}}}$. The corresponding received signal matrix can be expressed as:

$$\boldsymbol{Y_{k,i}} = \boldsymbol{H_{k,i}}\boldsymbol{P_{k,i}} + \boldsymbol{W_{k,i}} \tag{21}$$

where $\boldsymbol{P_{k,i}} = [\boldsymbol{p_{1_{k,i}}}, \ldots, \boldsymbol{p_{J_{k,i}}}]$ is the $2 \times J$ training symbol matrix, $\boldsymbol{Y_{k,i}} = [\boldsymbol{y_{1_{k,i}}}, \ldots, \boldsymbol{y_{J_{k,i}}}]$ is the corresponding $2 \times J$ matrix of received training symbols, and $\boldsymbol{W_{k,i}} = [\boldsymbol{w_{1_{k,i}}}, \ldots, \boldsymbol{w_{J_{k,i}}}]$ is the $2 \times J$ noise matrix. $\boldsymbol{p_{m_{k,i}}}$, $\boldsymbol{y_{m_{k,i}}}$, and $\boldsymbol{w_{m_{k,i}}}$ are all 2×1 vectors where $m = 1,2, \ldots, J$. An estimate of $\boldsymbol{H_{k,i}}$ can be now estimated using the least squares (LS) approach [37]:

$$\widehat{\boldsymbol{H}}_{\boldsymbol{k,i_{LS}}} = \boldsymbol{Y_{k,i}}\boldsymbol{P_{k,i}^{\dagger}} \tag{22}$$

where $\boldsymbol{P_{k,i}^{\dagger}} = \boldsymbol{P_{k,i}^{H}}\left(\boldsymbol{P_{k,i}}\boldsymbol{P_{k,i}^{H}}\right)^{-1}$ is the pseudo-inverse of $\boldsymbol{P_{k,i}}$. $(\cdot)^{H}$ denotes the Hermitian transpose, and $(\cdot)^{\dagger}$ represents a pseudo-inverse operation.

As an estimate of $\boldsymbol{H_{k,i}}$ is now known, the zero-forcing (ZF) estimate [38] of the transmitted data symbols is:

$$\widehat{\boldsymbol{x}}_{\boldsymbol{k,i_{ZF}}} = \widehat{\boldsymbol{H}}_{\boldsymbol{k,i_{LS}}}^{\dagger}\boldsymbol{y_{k,i}} \tag{23}$$

where $\widehat{\boldsymbol{H}}_{\boldsymbol{k,i_{LS}}}^{\dagger}$ is the pseudo-inverse of the estimated channel coefficients matrix $\widehat{\boldsymbol{H}}_{\boldsymbol{k,i_{LS}}}$.

IV. Experimental Results

A. Experimental System Setup

Fig. 4 shows the experimental setup where a dual-arm IQ soft-ROADM drop element is employed for signal recovery. The key system parameters are listed in Table I.

In the BBU/OLT-based transmitter, 6 (3I+3Q) SBs occupying 3 SW-bands are digitally combined and converted into an analogue electrical signal using the first channel of an arbitrary waveform generator (AWG, Keysight-M8195A) operating at 32 GS/s@8-bit with an amplitude of 0.7 Vpp. The Hilbert-pair approach is adopted to construct three digital filter pairs with a zero excess of bandwidth and a filter length of 32. The central frequencies of the three digital filter pairs satisfy Eq. (3) with $i = 2, 3, 4$, i.e., 3 GHz, 5 GHz, and 7 GHz.

For each SB signal, a real-valued digital orthogonal frequency-division multiplexing (OFDM) signal containing 12 16-QAM-encoded data-carrying subcarriers is generated using a 32-point inverse fast Fourier transform (IFFT). Hermitian symmetry is employed at the IFFT input to produce a real-valued signal, which is digitally up-sampled by a factor of $M = 8$, the resultant signal is then filtered by an appropriate I/Q Hilbert-pair-based shaping filter to locate the SB signal at the desired I or Q SB spectral region. All SBs signals are then digitally combined. Prior to digital-to-analogue conversion in the AWG, the total resultant signal is oversampled by a factor of 2 to constrain the signal bandwidth to be within 2GHz – 8GHz, thus the effective DAC sampling speed is $f_{DAC} = 16\ GS/s$. The baseband frequency region is kept free to be occupied with the dropped TSB.

To perform electrical-to-optical (E-O) conversion, a 35 GHz integrated optical transmitter (Thorlabs MX35D) is employed, which consists of an RF amplifier, a tuneable laser source, and a lithium niobate (LiNbO3) Mach-Zehnder Modulator (MZM) with a bias controller. The wavelength of the optical signal is

TABLE I
LIST OF PARAMETERS

Parameter	Value
DAC sample rate	32 GS/s
ADC sample rate	4 GS/s
Effective signal sample rate f_{DAC}	16 GS/s
Effective signal sample duration T_s	62.5 ns
DAC/ADC resolution	8 bits / 10 bits
Bandwidth of SW-band (without drop operation)	2 GHz
Bandwidth of SW-band (after drop operation)	1 GHz
IFFT/FFT size	32
Digital filter length	32
Digital filter roll-off factor	0
Up-sampling factor (M)	8
Number of data carrying subcarriers per sub-band	12
Modulation format	16 QAM
Cyclic prefix	12.5%
Clipping level	14 dB
Operating wavelength	1550.517 nm
Bit rate per sub-band	2.67 Gb/s
Total bit rate	16 Gb/s
PIN detector bandwidth	40 GHz
PIN detector responsivity	0.7 A/W
MZM bandwidth	10 GHz
MZM RF V_π @ 1 GHz	5.6 V
MZM DC bias RF V_π @ 1 KHz	6.5 V
MZM maximum RF port input power	24 dBm
Optical launch power	6 dBm

fixed at ~1550.517 nm. The optical power launched into different lengths of standard single-mode fiber (SSMF) is fixed at 6 dBm. After the SSMF, an Erbium-doped fiber amplifier (EDFA) is used to boost the optical signal power, and a tuneable optical band-pass filter (OBPF) is employed to filter out the out-of-band noise. The optical signal power at the output of the OBPF is set to 8.7 dBm.

To generate the I and Q drop RF signals required for the dual-arm IQ drop element, the second channel of the AWG is employed to generate a single-tone signal with the desired frequency (3 GHz, 5 GHz, or 7 GHz) and phase offset θ_{RF_i}. A common RF delay line is then employed to fine-tune the phase offset. An electrical power splitter (PS) is then employed to split the RF signal into two paths (I and Q), where each signal is individually amplified. An RF delay line is employed only in the second path (Q) to achieve the required 90° phase shift. To intentionally demonstrate the tolerance to received I/Q signal power imbalance, different drop RF signal powers are employed on the I and Q arms. It is important to highlight that all drop RF signal powers are within the linear region of the employed MZMs, and near the optimum level of the drop RF signal power of ~20 dBm for the adopted MZMs (determined by removing the PS). Thus, a slightly better performance can potentially be attained if drop RF signal powers of ~20 dBm are used, this was not possible during the experiment due to the available RF amplifiers. Table II lists the adopted powers of the drop RF signals.

TABLE II
POWER OF DROP RF SIGNALS

Signal Frequency	Signal Phase	Signal Power (dBm)
3 GHz	I/Q	15.5/17.8
5 GHz	I/Q	15.9/18.4
7 GHz	I/Q	15/17

In the dual-arm IQ drop element, a 3 dB optical splitter is utilized to direct the received optical signal into the two arms. Two 10 GHz MZMs (Thorlabs LN81S-FC) optimally biased at their quadrature bias points are then employed to perform I and Q drop operations. A suitably adjusted polarization controller (PC) is employed before each MZM to optimise performance. In each arm of the dual-arm IQ drop element, an optical splitter is utilized after the MZM to tap off 1% of the optical power for monitoring purposes, and a variable optical attenuator (VOA) followed by a 40 GHz PIN detector (Thorlabs RXM40AF) are employed for optical signal power control and O-E signal conversion respectively. A 13dB-gain RF amplifier and a 1 GHz LPF are then employed to amplify the signal and remove the ruined SBs and out-of-band noise. The received electrical signals from both arms are then digitized by a digital sampling oscilloscope (Keysight UXR0402A) operating at 4 GS/s@10-bit. Both digital signals are then processed offline for either individual I/Q detection to represent single-arm I/Q drop elements or jointly detected using the proposed MIMO-based I/Q crosstalk mitigation technique using the dual-arm IQ drop element shown in Fig. 3.

Due to the MZM's bandwidth limitation, a per SB bit rate of 2.67 Gb/s is achieved here. It is worth highlighting that as DFM-based systems have demonstrated per SB bit rates of >20 Gb/s [39], the soft-ROADM has the potential of supporting high capacity connectivity requirements in future 5G/6G networks.

Considering an optical back-to-back (OBTB) connection, Fig. 5(a) shows the electrical signal spectra if O-E conversion is performed at the input of the drop operation, the spectrum indicates the corresponding physical channel frequency response is reasonably flat. Fig. 5(b) shows the electrical signal spectra after dropping the I/Q SB and directly after O-E conversion, for the 2nd SW-band. It can be seen that the soft-ROADM drop operation shifts the TSB to the baseband region, whereas the other n-TSBs are ruined and unrecoverable. Fig. 5(c) illustrates the electrical signal spectra after the RF amplifier and the LPF, where the ruined SBs' signals are effectively removed by LP filtering. Due to the limited shaping filter tap count, and for reducing the impact of the unwanted subcarrier-subcarrier-intermixing (SSI) effect [29], three low-frequency data-carrying subcarriers are deactivated in each SB, this causes the occurrence of the power dips shown in Fig. 5(a).

Although theoretically, the ADC in the soft-ROADM drop elements can work at the TSB signal bandwidth (2 GS/s), an ADC sampling speed of 4 GS/s is chosen to reduce the aliasing effects due to the non-ideal frequency response of the employed LPF as illustrated in Fig. 5(c). A digital-domain down-sampling operation by a factor of 2 is thus performed after 1 GHz digital filtering and symbol alignment to achieve a 2 GS/s digital signal for data recovery.

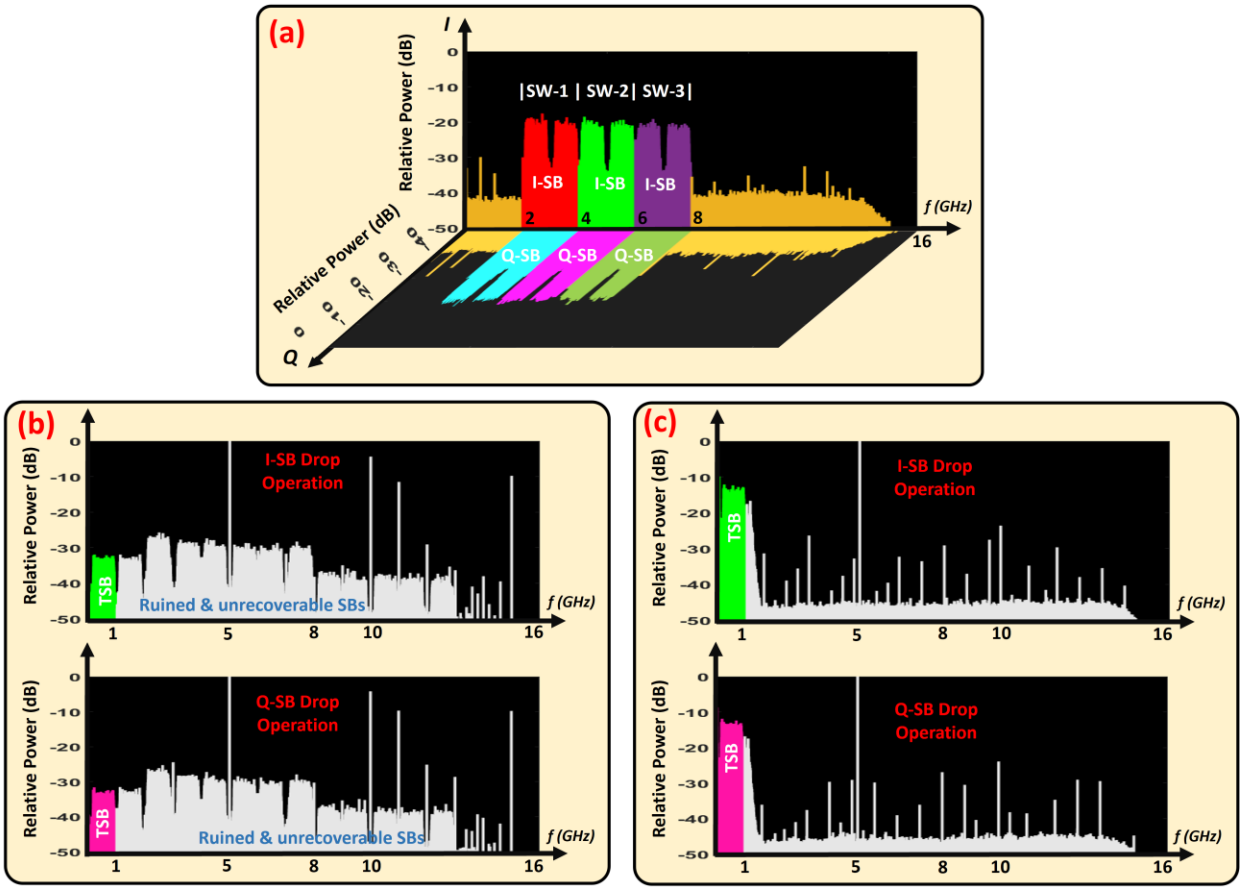

Fig. 5. Optical back-to-back electrical signal spectra of (a) the signal without the drop operation, (b) the signal after dropping I/Q SB in the 2nd SW-band (before RF amplifier and LPF), (c) the signal after dropping I/Q SB in the 2nd SW-band (after RF amplifier and LPF).

B. Downstream Performance Analysis

Utilizing the above-stated experimental setup and signal generation/demodulation procedures, the downstream BER versus received optical power (ROP) performances of all SBs for an OBTB connection are illustrated in Fig. 6, where the drop RF signal phase offset is set to the optimum value of $\theta_{RF_i} = 0$. For a fair comparison between single-arm and dual-arm soft-ROADM drop elements, the ROP always indicates the optical power at the input of the PIN detector(s).

The results demonstrate the ability to recover any SB using both the traditional single-arm and the newly proposed dual-arm soft-ROADM drop elements and that all SBs show similar BER developing trends. This indicates that the soft-ROADM drop operation's performance is independent of the SB/SW-band spectral location. Additionally, For the adopted forward error correction (FEC) limit of 3.8×10^{-3}, which corresponds to a 6.7% overhead (OH) hard-decision (HD)-FEC threshold [40], [41], lower frequency SBs show very slightly better sensitivity and lower BER floor compared with the higher frequency SBs due to the frequency response of the system.

As the drop RF signal phase offset θ_{RF_i} is intentionally adjusted to the optimum value during the drop operation, this prevents any I/Q crosstalk. Therefore, this suggests that, under the ideal conditions of zero phase offset, both the single-arm and the newly proposed dual-arm drop element architectures show similar performances.

C. Robustness to Fiber Transmission Channel

To properly evaluate and compare the robustness of the single-arm and the dual-arm drop elements to fiber-induced distortions and physical channel frequency response roll-off effects, a 50 km SSMF fiber transmission channel is considered to intensify the aforementioned effects. Fig. 7 shows the performance of soft-ROADM drop elements after 50 km SSMF transmissions, with $\theta_{RF_i} = 0$.

Compared with the OBTB results, the introduction of a 50 km SSMF fiber channel increases the noise floor of all SBs. The receiver sensitivities of the lowest frequency SBs are not highly affected by the fiber channel, and the fiber-induced optical power penalty is negligible. Whilst the sensitivities of the middle and highest frequency SBs are affected due to the strong fiber-induced frequency response roll-off effect as can be clearly seen in Fig. 8.

In addition, compared with the single-arm I/Q drop element, the dual-arm IQ drop element always shows a lower BER performance/floor and has an improved ability to mitigate fiber channel-induced distortions. For example, considering the highest frequency SBs, the single-arm I/Q drop element fails to achieve a BER below the FEC limit. Whereas the dual-arm IQ drop element is able to achieve the minimum required BER with an optical power penalty of 1.5 dB.

Overall, the results in Fig. 7 are clear evidence that the proposed dual-arm IQ drop element outperforms the single-arm

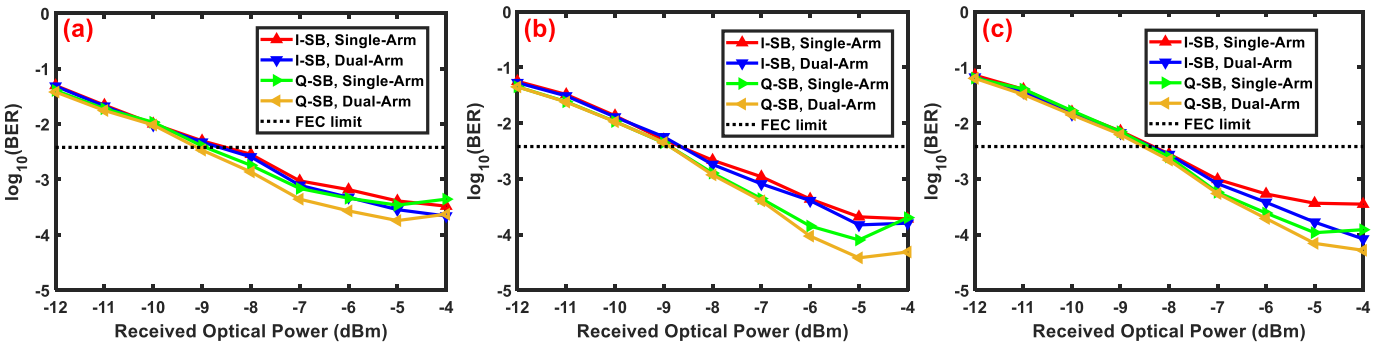

Fig. 6. OBTB BER performance of soft-ROADM drop elements, (a) SW-band 1, (b) SW-band 2, (c) SW-band 3.

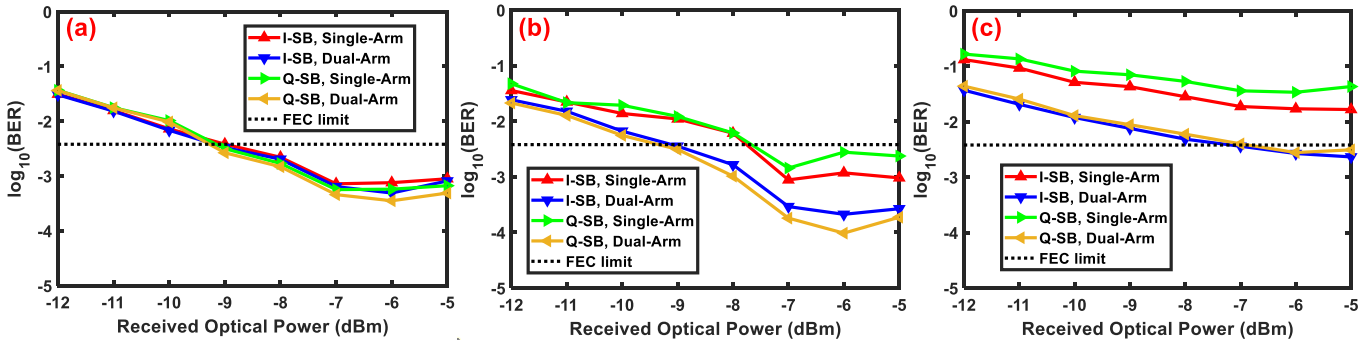

Fig. 7. BER performance of soft-ROADM drop elements after 50 km fiber channel, (a) SW-band 1, (b) SW-band 2, (c) SW-band 3.

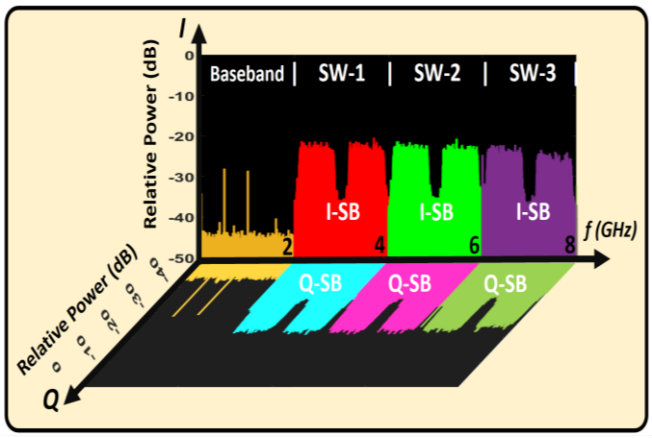

Fig. 8. Electrical signal spectra (without the drop operation) after 50 km fiber transmission channel.

I/Q drop element in mitigating the I/Q crosstalk due to channel-induced frequency response roll-off effects.

D. Robustness to Drop RF Signal Phase Offset

To explore the robustness of the soft-ROADM drop elements to the drop RF signal phase offset, the BER performance is monitored whilst the drop RF signal phase offset θ_{RF_i} is varied, and the received optical power is kept fixed. The results of the SBs occupying the 2nd (middle) SW-band are presented as this SW-band is bordered by the other two SW-bands. However, very similar results are observed for all SW-bands.

Fig. 9(a) (Fig. 9(b)) shows the effect of drop RF signal phase offset on the performance of the dropped I-SB (Q-SB) of the 2nd SW-band when only 3 I (Q) SBs are occupied without the existence of the Q (I) SBs. The ROP is set to -7 dBm. As only 3-I or 3-Q SBs are considered without the existence of the other spectrally overlapped SBs, there is no SB leakage, thus the drop RF signal phase offset causes OSNR degradation in the dropped TSB due to power loss only.

It can be seen in Figs. 9(a) and 9(b) that, when the single-arm I/Q drop element is employed, the impact of the phase-offset-induced power loss on the BER performance is minimum (maximum) at $\theta_{RF_i} \approx 0, \pm\pi$ ($\theta_{RF_i} \approx \pm\pi/2$) which agrees with Eqs. (13) and (14). It is also observed that, for the single-arm I/Q drop element, under the given conditions, the drop RF signal phase offset dynamic range to maintain BERs below the adopted FEC limit is $\sim \pm\pi/4$ for both SBs. However, it should be noted that the drop RF signal phase offset dynamic range is also dependent on the ROP level of the TSB.

In contrast, the proposed dual-arm IQ drop element demonstrates an excellent ability in mitigating the impact of phase-offset-induced power loss and always shows, for the given conditions, a BER below the FEC limit as illustrated in Figs. 9(a) and 9(b). In addition, the Q-arm has a higher drop RF signal power than the I-arm, therefore, Fig. 9(a) shows that I-SB has lower (higher) BER at $\theta_{RF_i} \approx \pm\pi/2$ ($\theta_{RF_i} \approx 0, \pm\pi$) where all I-SB signal power is received by the Q-arm (I-arm). In contrast, Q-SB in Fig. 9(b) has lower (higher) BER at $\theta_{RF_i} \approx 0, \pm\pi$ ($\theta_{RF_i} \approx \pm\pi/2$) where all Q-SB signal is received by the Q-arm (I-arm).

It is important to highlight the fact that the proposed dual-arm IQ drop element shows excellent phase-offset-insensitive BER performance when only either 3-I or 3-Q SBs are considered, which is clear evidence that, in order to operate, the proposed technique does not require both orthogonal I and Q SBs to be occupied.

Fig. 10 shows the impact of the drop RF signal phase offset on the performance of the dropped I and Q SBs of the 2nd SW-

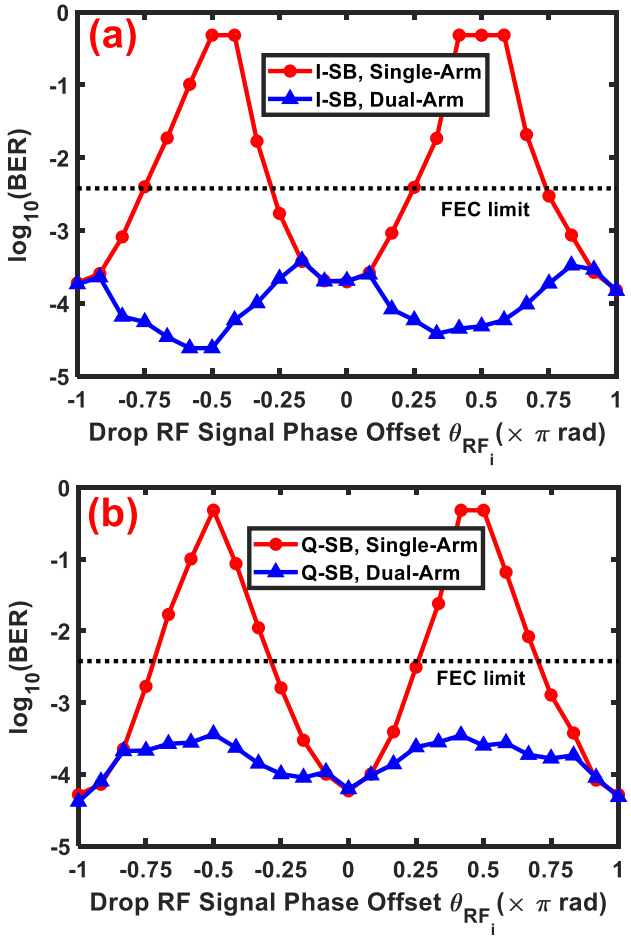

Fig. 9. The effect of drop RF signal phase offset when (a) only 3-I SBs are occupied, (b) only 3-Q SBs are occupied.

band when all 6 SBs are occupied at a fixed ROP of -7 dBm. Compared with Fig. 9, it is noted that, the impact of drop RF signal phase offset on the performance of the single-arm I/Q drop element is higher in the presence of both spectrally overlapped orthogonal SBs due to the additional leakage terms in Eqs. (13) and (14). For the given conditions, to maintain BERs below the adopted FEC limit, and for a fixed ROP of -7 dBm, the observed drop RF signal phase offset dynamic range in the single-arm I/Q drop element is only $< \pm 0.05\pi$. Although this drop RF signal phase offset dynamic range is ROP-dependent, the ratio of leakage power to wanted power is ROP-independent and fixed for a given drop RF signal phase offset.

In contrast, due to the ability of the proposed dual-arm IQ drop element to mitigate the I/Q crosstalk effects, it always achieves a BER below the FEC limit regardless of the drop RF signal phase offset. The BER performances of both SBs in the dual-arm IQ drop element oscillate in opposite directions as the drop RF signal phase offset varies, this is mainly due to:

1) Varying the drop RF signal phase offset changes the distribution/ratio of both wanted and unwanted SBs' powers at the output of each arm. As the Q-arm has a higher drop RF signal power than I-arm, this causes Q-SB (I-SB) to have lower BER performance than I-SB (Q-SB) at $\theta_{RF_i} \approx 0, \pm\pi$ ($\theta_{RF_i} \approx \pm\pi/2$).

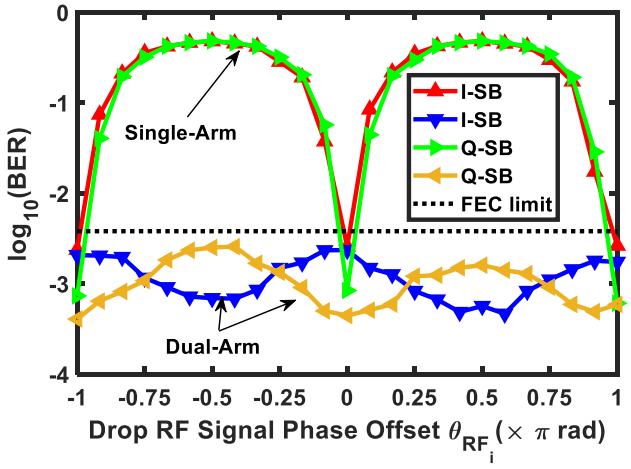

Fig. 10. The effect of drop RF signal phase offset when 3-I + 3-Q SBs are occupied.

2) Independent MZMs are employed in each arm, and since each MZM is manually biased at its quadrature point, any drift/error in the actual bias point from the optimum value can cause I and Q SBs to have different BER performances.
3) Independent PIN detectors and LPFs are employed in each arm, which can have slightly different noise/distortion characteristics.

However, the fact that the BER performance of both SBs is always maintained below the FEC limit validates the effectiveness of the proposed dual-arm IQ drop element in mitigating the impacts of drop RF signal phase offset. This drastically increases the technical feasibility of soft-ROADMs for application in optical-wireless converged access networks, as the need to accurately control the drop RF signal phase is completely eliminated.

E. Robustness to Channel-Induced STO

As the channel-induced STO has a similar impact to the drop RF signal phase offset, it is very important to evaluate the effectiveness of the proposed dual-arm IQ drop element in mitigating the impact of the channel-induced STO, Fig. 11(a) shows the effect of integer STO increments on the performance of the SBs in the 2nd SW-band at a fixed ROP of -7 dBm and $\theta_{RF_i} = 0$. The presented integer STO is normalized to the effective DAC sampling time interval T_s where $T_s = (1/f_{DAC})$. The integer STO is introduced using the AWG-embedded sample delay function.

It can be seen in Fig. 11(a) that the single-arm I/Q drop element is very sensitive to STO, as the BER dips occur every 8 samples within the cyclic prefix (CP) inter-symbol interference (ISI) margin, which corresponds to an STO-induced phase offset θ_{STO_i} of $0, -5\pi, -10\pi, -15\pi$ (i.e., $0\pi, -\pi$) using:

$$\theta_{STO_i} = -2\pi f_{c_i} \delta T_s \tag{24}$$

where δ is the normalized STO relative to T_s.

In contrast, an excellent ability in mitigating the impact of channel-induced STO within the CP-ISI margin is observed in the dual-arm IQ drop element case. The performances of both I

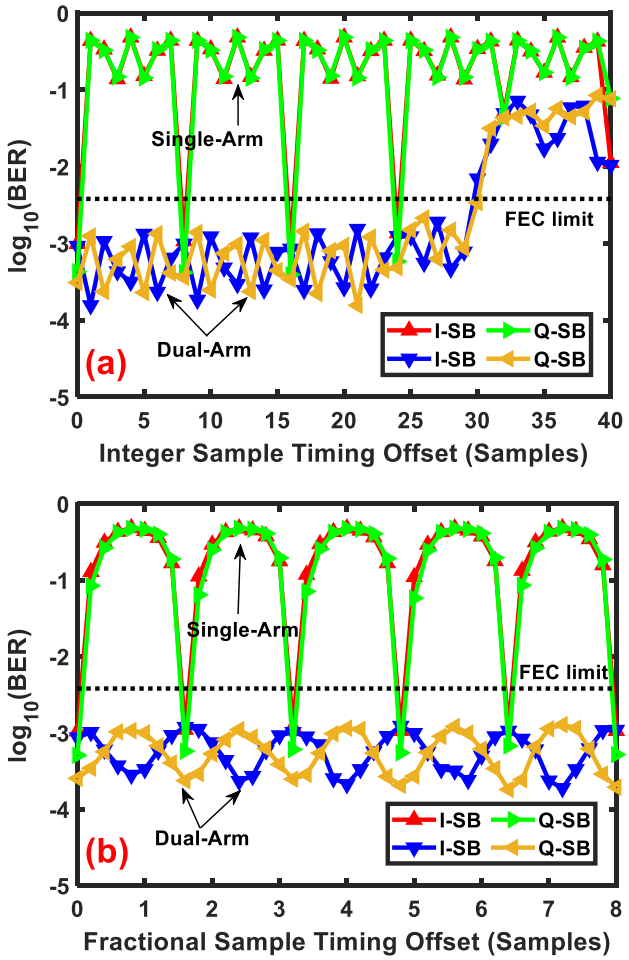

Fig. 11. The effect of channel-induced STO on BER performance. (a) integer sample timing offset, (b) fractional sample timing offset.

and Q SBs slightly oscillate in opposite directions since the STO has the same effect as the drop RF signal phase offset, thus the STO varies the power distribution of I and Q SBs in both arms of the dual-arm IQ drop element. It should be noted that the channel-induced STO will also influence the corresponding STO at the input to the DSP receiver, but this is compensated by the symbol alignment function shown in Fig. 3.

As the BER performance of the single-arm I/Q drop element forms a repeating pattern that repeats every 8 samples within the CP-ISI margin, Fig. 11(b) investigates the effect of fractional STO over an interval of 0 – 8 samples, with a sample resolution of 0.2 samples. The fractional STO is implemented using a variable optical delay line after the OBPF and before the optical coupler in Fig. 4.

The finer delay resolution in Fig. 11(b) reveals the extreme sensitivity of the single-arm I/Q drop element to the STO as the resultant BER is always high with dips that occur every 1.6 samples, which translates to every $-\pi$ radians when considering the corresponding phase offset, using Eq. (24). For the SBs of the 1st (3rd) SW-band, within the same STO range, the resultant BER is also always high but with 4 (8) BER dips as the STO-induced phase offset θ_{STO_i} is frequency-dependent.

It should be highlighted that, the observed BER dips in Figs. 11(a) and 11(b), which shows the ability of the single-arm I/Q drop element to handle any θ_{STO_i} (or θ_{RF_i}) of $\pm n\pi$ (where $n = 1,2,3, ...$) are only because I/Q crosstalk effects are minimum at these points as can be concluded from Eqs. (13) and (14).

The dual-arm IQ drop element, however, can overcome the impact of any fractional STO, as for the given conditions, the BER is maintained below the FEC limit as STO is varied. This consequently removes the requirement of stringent timing adjustment and/or drop RF signal phase control in the dual-arm IQ drop elements, which is however clearly necessary for single-arm I/Q drop elements.

F. Performance Stability Over Time

It is important to highlight that all the previous experimental demonstrations of the single-arm I/Q drop element in [27]–[29] were all based on an OBTB connection and did not consider a fiber transmission channel. In addition, the stability of the BER performance of the single-arm I/Q drop element has not been investigated previously. However, the propagation delay of the optical signal through the fiber may vary over time due to effects such as the temperature sensitivity of the fiber propagation delay, and wavelength drift of the transmitter's laser source, consequently, the relative signal timing at the receiver is almost always time-dependent. It is therefore vital to observe the system performance stability of soft-ROADM drop elements over a sufficiently long period. Fig. 12 shows the performance stability of the soft-ROADM drop elements over a 30-minute period where the BER is monitored every 30 seconds. The ROP is kept fixed at -5 dBm and a fiber transmission channel of 10.7 km SSMF is considered.

As the single-arm I/Q drop element is very sensitive to timing effects, the BER performance of all SBs degrades quickly within the first two minutes, whereas the proposed dual-arm IQ drop element always achieves a BER below the adopted FEC limit, thus achieving excellent performance stability.

It is interesting to note that, the rate of drift in BER depends on i) the propagation delay timing drift due to environmental conditions such as temperature and ii) the SW-band centre frequency, as time shift translates to a phase offset which is frequency-dependent. The BER trends varied with each experimental observation as the temperature effect is quite dominant, however it is evident that the SBs occupying the 1st SW-band show a slower BER drift as expected. The periodicity in the BER trends is due to the time shift translating to an effective phase offset, and BER is periodic with phase offset as shown in Figs. 9 and 10.

Overall, the results are clear evidence of the excellent technical feasibility of the proposed dual-arm IQ drop element architecture compared with the single-arm solution.

V. Conclusions

A dual-arm soft-ROADM drop operation with phase-offset-insensitive performance, is experimentally demonstrated using a DSP implemented MIMO-based I/Q crosstalk mitigation technique, thus eliminating the need to dynamically control the drop RF signal phase offset, which is necessary for a single-arm I/Q drop element.

This work also shows that the newly proposed dual-arm IQ

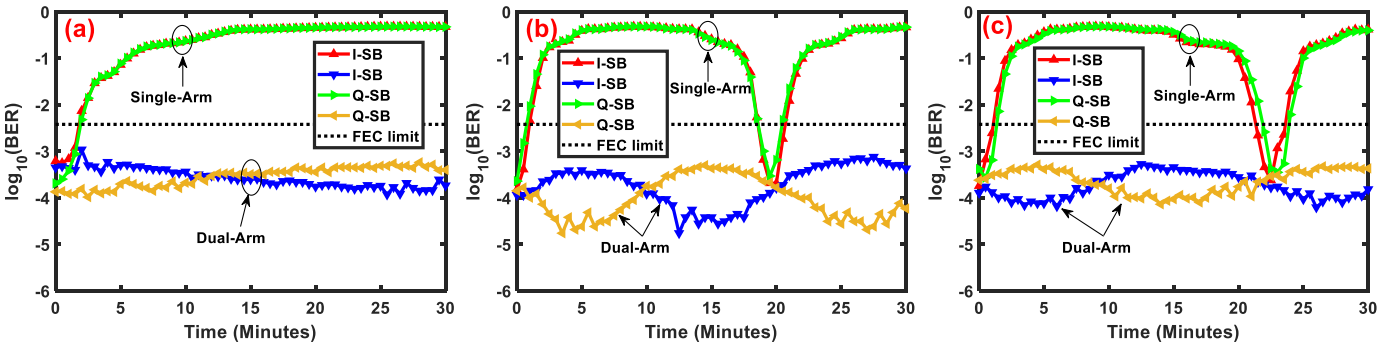

Fig. 12. BER performance of soft-ROADM drop elements observed over 30 minutes time period, (a) SW-band 1, (b) SW-band 2, (c) SW-band 3.

drop element significantly outperforms the previously reported single-arm I/Q drop element in mitigating I/Q crosstalk effects caused as a result of, the fiber transmission channel-induced frequency response roll-off, STO timing errors between the transmitter and the receiver, and the continuous time-varying propagation delay drifting effects.

In addition, in contrast to the single-arm I/Q drop element which shows poor BER performance stability, the proposed dual-arm IQ drop element demonstrates excellent BER stability.

Soft-ROADMs based on the dual-arm IQ drop element, therefore, offer a potential low-cost solution to enable flexible optical-wireless converged access networks.

REFERENCES

[1] L. Banda, M. Mzyece, and F. Mekuria, "5G Business Models for Mobile Network Operators—A Survey," *IEEE Access*, vol. 10, pp. 94851–94886, 2022, doi: 10.1109/ACCESS.2022.3205011.

[2] J. Xia *et al.*, "A Future Proof Reconfigurable Wireless and Fixed Converged Optical Fronthaul Network Using Silicon Photonic Switching Strategies," *J. Lightw. Technol.*, vol. 41, no. 6, pp. 1610–1618, Mar. 2023, doi: 10.1109/JLT.2022.3188773.

[3] Z. Zhang *et al.*, "6G Wireless Networks: Vision, Requirements, Architecture, and Key Technologies," *IEEE Veh. Technol. Mag.*, vol. 14, no. 3, pp. 28–41, Sep. 2019, doi: 10.1109/MVT.2019.2921208.

[4] X. Liu and F. Effenberger, "Emerging Optical Access Network Technologies for 5G Wireless," *J. Opt. Commun. Netw.*, vol. 8, no. 12, pp. B70–B79, Dec. 2016, doi: 10.1364/JOCN.8.000B70.

[5] J. Kani, J. Terada, K.-I. Suzuki, and A. Otaka, "Solutions for future mobile fronthaul and access-network convergence," *J. Lightw. Technol.*, vol. 35, no. 3, pp. 527–534, Feb. 2017, doi: 10.1109/JLT.2016.2608389.

[6] S. Sarmiento, J. A. Altabas, D. Izquierdo, I. Garces, S. Spadaro, and J. A. Lazaro, "Cost-Effective DWDM ROADM Design for Flexible Sustainable Optical Metro–Access Networks," *J. Opt. Commun. Netw.*, vol. 9, no. 12, pp. 1116–1124, Dec. 2017, doi: 10.1364/JOCN.9.001116.

[7] C. Browning *et al.*, "A Silicon Photonic Switching Platform for Flexible Converged Centralized-Radio Access Networking," *J. Lightw. Technol.*, vol. 38, no. 19, pp. 5386–5392, Oct. 2020, doi: 10.1109/JLT.2020.2984379.

[8] M. Ruffini *et al.*, "Access and Metro Network Convergence for Flexible End-to-End Network Design [Invited]," *J. Opt. Commun. Netw.*, vol. 9, no. 6, pp. 524–535, Jun. 2017, doi: 10.1364/JOCN.9.000524.

[9] D. Welch *et al.*, "Point-to-Multipoint Optical Networks Using Coherent Digital Subcarriers," *J. Lightw. Technol.*, vol. 39, no. 16, pp. 5232–5247, Aug. 2021, doi: 10.1109/JLT.2021.3097163.

[10] P. Sarigiannidis, T. Lagkas, S. Bibi, A. Ampatzoglou, and P. Bellavista, "Hybrid 5G optical-wireless SDN-based networks, challenges and open issues," *IET Netw.*, vol. 6, no. 6, pp. 141–148, Nov. 2017, doi: 10.1049/iet-net.2017.0069.

[11] M. Ruffini, F. Slyne, C. Bluemm, N. Kitsuwan, and S. McGettrick, "Software Defined Networking for Next Generation Converged Metro-Access Networks," *Opt. Fiber Technol.*, vol. 26, pp. 31–41, Dec. 2015, doi: 10.1016/j.yofte.2015.08.008.

[12] T. -K. Kang, B. -S. Joo, J. -H. Lee, and H. -J. Kim, "Switching system architecture for optical-circuit-packet converged transport network," in *2014 12th International Conference on Optical Internet 2014 (COIN)*, Jeju: IEEE, Aug. 2014, pp. 1–2. doi: 10.1109/COIN.2014.6950609.

[13] G. Kalfas *et al.*, "Next Generation Fiber-Wireless Fronthaul for 5G mmWave Networks," *IEEE Commun. Mag.*, vol. 57, no. 3, pp. 138–144, Mar. 2019, doi: 10.1109/MCOM.2019.1800266.

[14] A. Tsakyridis *et al.*, "Reconfigurable Fiber Wireless IFoF Fronthaul With 60 GHz Phased Array Antenna and Silicon Photonic ROADM for 5G mmWave C-RANs," *IEEE J. Sel. Areas Commun.*, vol. 39, no. 9, pp. 2816–2826, Sep. 2021, doi: 10.1109/JSAC.2021.3064649.

[15] H. Yang, B. Robertson, P. Wilkinson, and D. Chu, "Low-Cost CDC ROADM Architecture Based on Stacked Wavelength Selective Switches," *J. Opt. Commun. Netw.*, vol. 9, no. 5, pp. 375–384, May 2017, doi: 10.1364/JOCN.9.000375.

[16] M. D. Feuer and S. L. Woodward, "Advanced ROADM Networks," in *Optical Fiber Communication Conference/National Fiber Optic Engineers Conference*, Los Angeles, California: OSA, 2012, p. NW3F.3. doi: 10.1364/NFOEC.2012.NW3F.3.

[17] B. C. Collings, "Advanced ROADM Technologies and Architectures," in *Optical Fiber Communication Conference*, Los Angeles, California: OSA, 2015, p. Tu3D.3. doi: 10.1364/OFC.2015.Tu3D.3.

[18] R. A. Jensen, "Optical Switch Architectures for Emerging Colorless/Directionless/Contentionless ROADM Networks," in *Optical Fiber Communication Conference/National Fiber Optic Engineers Conference 2011*, Los Angeles, California: OSA, 2011, p. OThR3. doi: 10.1364/OFC.2011.OThR3.

[19] P. Roorda and B. Collings, "Evolution to Colorless and Directionless ROADM Architectures," in *2008 Conference on Optical Fiber Communication/National Fiber Optic Engineers Conference*, San Diego, CA, USA: IEEE, Feb. 2008, pp. 1–3. doi: 10.1109/OFC.2008.4528321.

[20] M. Bolea, R. P. Giddings, M. Bouich, C. Aupetit-Berthelemot, and J. M. Tang, "Digital filter multiple access PONs with DSP-enabled software reconfigurability," *J. Opt. Commun. Netw.*, vol. 7, no. 4, pp. 215–222, Apr. 2015, doi: 10.1364/JOCN.7.000215.

[21] X. Zhou, W. Jia, Y. Ma, N. Deng, G. Shen, and A. Lord, "An Ultradense Wavelength Switched Network," *J. Lightw. Technol.*, vol. 35, no. 11, pp. 2063–2069, Jun. 2017, doi: 10.1109/JLT.2016.2642119.

[22] G. Shen *et al.*, "Ultra-Dense Wavelength Switched Network: A Special EON Paradigm for Metro Optical Networks," *IEEE Commun. Mag.*, vol. 56, no. 2, pp. 189–195, Feb. 2018, doi: 10.1109/MCOM.2018.1700025.

[23] Y. Zhang, X. Zhou, N. Deng, and G. Shen, "Ultra Dense-Wavelength Switched Network (UD-WSN): A Cost, Energy, and Spectrum Efficient Metro Network Architecture," in *Asia Communications and Photonics Conference 2016*, Wuhan: OSA, 2016, p. AF4D.3. doi: 10.1364/ACPC.2016.AF4D.3.

[24] W. Jin *et al.*, "Improved Performance Robustness of DSP-Enabled Flexible ROADMs Free from Optical Filters and O-E-O Conversions," *J. Opt. Commun. Netw.*, vol. 8, no. 8, pp. 521–529, Aug. 2016, doi: 10.1364/JOCN.8.000521.

[25] W. Jin *et al.*, "DSP-Enabled Flexible ROADMs Without Optical Filters and O-E-O Conversions," *J. Lightw. Technol.*, vol. 33, no. 19, pp. 4124–4131, Oct. 2015, doi: 10.1109/JLT.2015.2470127.

[26] W. Jin *et al.*, "OSNR Penalty-Free Add/Drop Performance of DSP-Enabled ROADMs in Coherent Systems," *J. Opt. Commun. Netw.*, vol. 9, no. 9, pp. 730–738, Sep. 2017, doi: 10.1364/JOCN.9.000730.

[27] M. L. Deng, X. Duan, W. Jin, R. P. Giddings, S. Mansoor, and J. M. Tang, "Experimental demonstration and performance evaluation of flexible add/drop operations of DSP-switched ROADMs for cloud access networks," *Opt. Commun.*, vol. 428, pp. 95–103, Dec. 2018, doi: 10.1016/j.optcom.2018.07.050.

[28] X. Duan, M. L. Deng, W. Jin, R. P. Giddings, S. Mansoor, and J. M. Tang, "Experimental Demonstration of DSP-enabled Drop Operations of Flexible ROADMs Excluding Optical Filters and O-E-O Conversions," in *Optical Fiber Communication Conference*, Anaheim, California: OSA, 2016, p. M3E.4. doi: 10.1364/OFC.2016.M3E.4.

[29] E. Al-Rawachy, R. P. Giddings, and J. M. Tang, "Real-time experimental demonstration of DSP-enabled soft-ROADMs with multi-level flexible add/drop functions for cloud access networks," *Opt. Express*, vol. 27, no. 1, pp. 16–33, Jan. 2019, doi: 10.1364/OE.27.000016.

[30] D. Welch *et al.*, "Digital Subcarrier Multiplexing: Enabling Software-Configurable Optical Networks," *J. Lightw. Technol.*, vol. 41, no. 4, pp. 1175–1191, Feb. 2023, doi: 10.1109/JLT.2022.3211466.

[31] M. Garrido, K. Moller, and M. Kumm, "World's Fastest FFT Architectures: Breaking the Barrier of 100 GS/s," *IEEE Trans. Circuits Syst. Regul. Pap.*, vol. 66, no. 4, pp. 1507–1516, Apr. 2019, doi: 10.1109/TCSI.2018.2886626.

[32] Y. Dong, R. P. Giddings, and J. Tang, "Hybrid OFDM-digital filter multiple access PONs," *J. Lightw. Technol.*, vol. 36, no. 23, pp. 5640–5649, Dec. 2018, doi: 10.1109/JLT.2018.2877840.

[33] P. Dong, K. W. Kim, A. Melikyan, and Y. Baeyens, "Silicon Photonics: a Scaling Technology for Communications and Interconnects," in *2018 IEEE International Electron Devices Meeting (IEDM)*, San Francisco, CA: IEEE, Dec. 2018, p. 23.4.1-23.4.4. doi: 10.1109/IEDM.2018.8614701.

[34] R. Sabella, "Silicon Photonics for 5G and Future Networks," *IEEE J. Sel. Top. Quantum Electron.*, vol. 26, no. 2, pp. 1–11, Mar. 2020, doi: 10.1109/JSTQE.2019.2948501.

[35] S. Coleri, M. Ergen, A. Puri, and A. Bahai, "Channel estimation techniques based on pilot arrangement in OFDM systems," *IEEE Trans. Broadcast.*, vol. 48, no. 3, pp. 223–229, Sep. 2002, doi: 10.1109/TBC.2002.804034.

[36] J.-J. van de Beek, O. Edfors, M. Sandell, S. K. Wilson, and P. O. Borjesson, "On channel estimation in OFDM systems," in *1995 IEEE 45th Vehicular Technology Conference. Countdown to the Wireless Twenty-First Century*, Chicago, IL, USA: IEEE, 1995, pp. 815–819. doi: 10.1109/VETEC.1995.504981.

[37] M. Biguesh and A. B. Gershman, "Training-based MIMO channel estimation: a study of estimator tradeoffs and optimal training signals," *IEEE Trans. Signal Process.*, vol. 54, no. 3, pp. 884–893, Mar. 2006, doi: 10.1109/TSP.2005.863008.

[38] C. Wang, E. Au, R. Murch, W. Mow, R. Cheng, and V. Lau, "On the Performance of the MIMO Zero-Forcing Receiver in the Presence of Channel Estimation Error," *IEEE Trans. Wirel. Commun.*, vol. 6, no. 3, pp. 805–810, Mar. 2007, doi: 10.1109/TWC.2007.05384.

[39] W. Jin *et al.*, "Experimental demonstrations of DSP-enabled flexibility, adaptability and elasticity of multi-channel >72Gb/s over 25 km IMDD transmission systems," *Opt. Express*, vol. 29, no. 25, pp. 41363–41376, Dec. 2021, doi: 10.1364/OE.440115.

[40] Y. Zhu, X. Ruan, K. Zou, and F. Zhang, "Beyond 200G Direct Detection Transmission With Nyquist Asymmetric Twin-SSB Signal at C-Band," *J. Lightw. Technol.*, vol. 35, no. 17, pp. 3629–3636, Sep. 2017, doi: 10.1109/JLT.2017.2718098.

[41] E. Berikaa, M. S. Alam, and D. V. Plant, "Beyond 300 Gbps Short-Reach Links Using TFLN MZMs With 500 mV_{pp} and Linear Equalization," *IEEE Photonics Technol. Lett.*, vol. 35, no. 3, pp. 140–143, Feb. 2023, doi: 10.1109/LPT.2022.3227085.